CHAPTER

2.3

Susceptibility Artifacts

Emine U. Saritas[1,2], *Samantha J. Holdsworth*[3], *Roland Bammer*[3]

[1]Department of Bioengineering, University of California, Berkeley, CA, USA

[2]Department of Electrical and Electronics Engineering, Bilkent University, Ankara, Turkey

[3]Center for Quantitative Neuroimaging, Department of Radiology, Stanford University, Stanford, CA, USA

2.3.1 INTRODUCTION: SOURCES OF SUSCEPTIBILITY ARTIFACTS

The uniformity of the B_0 main field in magnetic resonance imaging (MRI) is critical for artifact-free image formation. MRI scanners are manufactured with a stringent requirement of less than one part-per-million (ppm)[a] variation in the B_0 field. However, this 1 ppm theoretical homogeneity easily gets distorted once a subject is placed inside the MRI scanner, mainly due to a 9 ppm magnetic susceptibility difference between air and tissue. The presence of any surgical implants further exacerbates the problem, as different tissue types, air, and metal all interact with and distort the applied magnetic field differently. This interaction is quantified by what is called the magnetic susceptibility of a matter.[1]

The susceptibility variations in tissue on a microscopic scale are in fact the source of many useful contrast mechanisms in MRI, such as blood oxygenation level-dependent (BOLD) functional MRI (fMRI) and diagnosis of cerebral hemorrhage. However, a macroscopic susceptibility variation leads to a global field inhomogeneity, which in turn creates off-resonance induced artifacts in the images. These artifacts manifest as faster T_2^* decay, signal dropouts and pileups, geometric distortions, and incomplete fat suppression. High-field MRI scans especially suffer from susceptibility artifacts, as the absolute size of the field perturbations increases linearly with B_0 field strength. For example, the 9 ppm susceptibility difference between air and tissue corresponds to a 575 Hz field variation at 1.5 T, while it is doubled to a 1150 Hz variation at 3 T. While a global frequency shift can be easily dealt with by adjusting the center frequency, it is the local field inhomogeneity that perturbs the imaging process.

In vivo MRI of the spinal cord is especially challenging due to susceptibility variations between various tissue types (e.g., vertebrae, muscle, CSF, gray and white matter, fat, air in the lungs and trachea, bowel gas, and surgical implants) that significantly distort the applied magnetic field. As shown by the B_0 field maps of the spine (Figure 2.3.1), the air in the lungs and nasal cavities as well as the curvature in the neck significantly distort the field around the spinal cord. Furthermore, susceptibility differences between vertebral spinous processes and connective tissue create local field inhomogeneities along the spinal cord itself, as seen in Figure 2.3.1(B). Bulk physiologic motion from cardiac and respiratory cycles, CSF pulsation, as well as breathing and swallowing further cause temporal variations of these field inhomogeneities.

This chapter gives an overview of susceptibility artifacts and how they manifest in EPI images of the spinal cord. Methods to alleviate these artifacts will be outlined. Please note that while this chapter mostly presents examples of susceptibility artifacts on sagittal images, axial and coronal orientations are equally affected.

2.3.2 ARTIFACTS IN EPI OF THE SPINAL CORD

Single-shot echo planar imaging (ss-EPI) remains the most frequently used technique for most of the quantitative imaging methods, because it acquires the whole of

[a]In MRI, the variations in B_0 field or the differences in resonant frequencies are so small that they are expressed in "parts per million", or ppm. For example, 1 ppm inhomogeneity at 1.5 T corresponds to a 1.5 μT variation in the B_0 field. This field variation would in turn result in a 63.87 Hz off-resonance (i.e., one-millionth of the center frequency of $f_0 = 63.87$ MHz at 1.5 T).

http://dx.doi.org/10.1016/B978-0-12-396973-6.00007-1

Copyright © 2014 Elsevier Inc. All rights reserved.

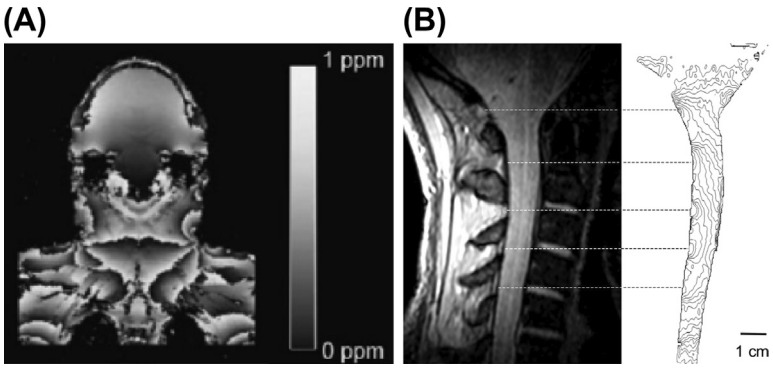

FIGURE 2.3.1 B_0 field maps of the cervical spine, showing over 6 ppm variation in field homogeneity. (A) The coronal view of the cervicothoracic area shows how the lungs and the nasal cavities contribute to field variations. Here, each phase wrap reflects a 1 ppm field change. (B) T_1-weighted sagittal view of the spinal cord and contour plot of the B_0 field map showing local distortions in magnetic field caused by susceptibility differences between vertebral spinous processes and connective tissue. Note how the regions shown with the dashed lines experience high distortion in the EPI image in Figure 2.3.2(C). Contour spacing = 10 Hz at 2 T field, or approximately 0.1 ppm. *Source: (A) from Reference 2; (B) obtained with permission from Ref. 3.*

k-space after a single excitation. This fast imaging capability is especially critical for methods that are sensitive to subject motion (e.g., diffusion-weighted imaging (DWI)) or for methods that require a high temporal resolution (e.g., fMRI).

Although ss-EPI performs relatively well in the brain, the anatomy of the spine as well as the abundance of susceptibility variations make it particularly difficult to produce high-quality ss-EPI images of the spinal cord. The long and narrow anatomy of the spine requires a large field of view (FOV) in the superior-inferior (S/I) direction, and the small cross-sectional size of the spinal cord mandates high-spatial-resolution images. Even in the axial imaging plane, where the spinal cord presents a small region of interest (ROI), the rest of the body dictates a large FOV. Covering a large FOV with high resolution requires long readout durations in EPI, which in turn result in distortions and severe blurring of the images along the phase-encoding (PE) direction. In addition, the long interval between subsequent *k*-space lines (i.e., echo spacing) causes significant image distortions due to off-resonance effects.

The location-dependent geometric distortion in an EPI image can be expressed as:

$$d_{\mathrm{PE}}(r) = \frac{\Delta f(r)\, T_{\mathrm{ESP}}\, \mathrm{FOV}_{\mathrm{PE}}}{N_{\mathrm{int}}\, R}. \qquad (2.3.1)$$

Here, $d_{PE}(r)$ is the local displacement of a voxel in the PE direction (i.e., the voxel appears at position $r + d_{PE}(r)$ instead of at r), $\Delta f(r)$ (in Hertz) represents a field inhomogeneity or off-resonance effect observed at position r, and FOV_{PE} is the FOV in the PE direction, T_{ESP} (in seconds) is the time interval between two adjacent echoes during an EPI readout (referred to as the "echo spacing"), N_{int} is the number of interleaves in EPI (e.g., $N_{int} = 1$ for ss-EPI), and R denotes the acceleration factor for parallel imaging (e.g., $R = 1$ for no acceleration). As seen in Eqn (2.3.1), a large FOV, increased readout duration due to a need for high resolution, and increased susceptibility variations all contribute to geometric distortions in EPI images. For example, a local 6 ppm off-resonance at 3 T, a $FOV_{PE} = 18$ cm, and $T_{ESP} = 0.5$ ms (all typical numbers in the spine) would cause close to 7 cm local displacement for regular ss-EPI. This level of distortion, as demonstrated in Figure 2.3.2(C), can easily render regular ss-EPI images clinically unusable.

ss-EPI images also exhibit a substantial water–fat misalignment, as the frequency term in Eqn (2.3.1) also applies to chemical shifts. For example, for the aforementioned imaging parameters, the fat image would experience a 4 cm shift in the PE direction with respect to the water image (assuming a chemical shift of 3.5 ppm, i.e., 440 Hz at 3 T). Hence, ss-EPI mandates proper shimming of the ROI, as well as a robust fat suppression or spectrally selective excitation.[4,5] These fat suppression schemes usually take advantage of the chemical shift (i.e., differences in resonant frequencies) between fat and water. Unfortunately, susceptibility variations around the spine can distort the field homogeneity to such an extent that effective fat suppression is often an issue. For example, a local 440 Hz susceptibility-induced off-resonance at 3 T would cause the water signal to be suppressed, instead of the fat signal. Figure 2.3.2(B) demonstrates this phenomenon, where the susceptibility variations around the cervical spine resulted in an incomplete fat suppression (white arrow) and a signal dropout (red arrow).

The position dependency of susceptibility effects causes different regions in the FOV to experience different levels of displacement, further complicating the problem. This nonrigid distortion is typically

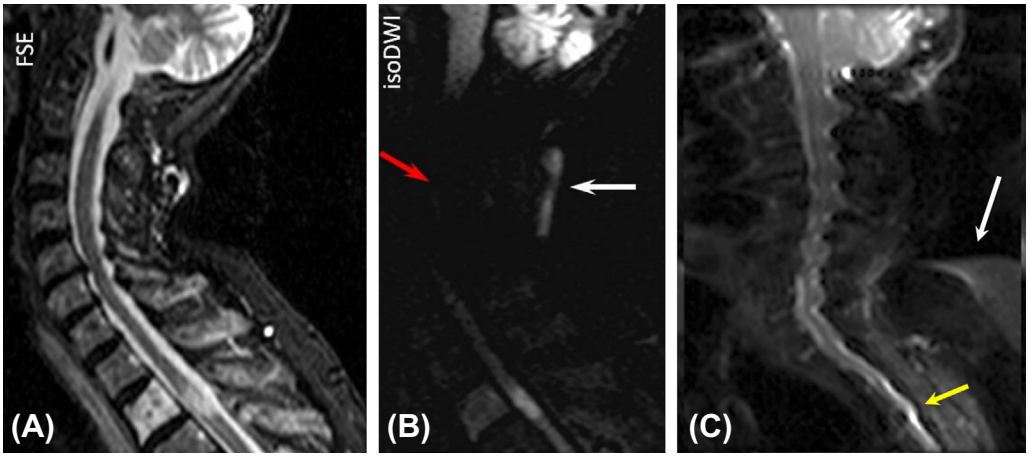

FIGURE 2.3.2 Various manifestations of susceptibility artifacts. (A) T_2-weighted fast spin-echo image showing the anatomy, and (B) corresponding isotropic diffusion-weighted image acquired using interleaved EPI. Susceptibility variations around the spine result in incomplete fat suppression (white arrow) and a signal drop (red arrow). (C) T_2-weighted single-shot EPI of the cervical spine demonstrates high levels of distortion, as well as incomplete fat suppression (white arrow). Local susceptibility differences between vertebral spinous processes and connective tissue, as shown in Figure 2.3.1(B), result in a comb-like appearance of the spine. In the cervicothoracic junction, the signals from the spinal cord and the CSF are piled up, while the neighboring pixels (where CSF was supposed to be) are left devoid of signal (yellow arrow).

observed as signal pileups or dropouts in an EPI image. The cervicothoracic junction in Figure 2.3.2(C) shows one such case, where the signals from the spinal cord and the CSF are piled up, while the neighboring pixels (where CSF was supposed to be) are left devoid of signal (yellow arrow). A less severe manifestation of this susceptibility artifact is the comb-like appearance of the spinal cord in Figure 2.3.2(C), which is caused by the local field inhomogeneities along the spinal cord (see Figure 2.3.1(B)).

2.3.3 METHODS TO REDUCE SUSCEPTIBILITY ARTIFACTS

There are various approaches that can be used to reduce susceptibility artifacts for spinal cord imaging; unfortunately, many of these methods have only been demonstrated in the research arena and are not available on clinical scanners. These approaches target one (or more) of the variables in Eqn (2.3.1), which can be rewritten as:

$$d_{\mathrm{PE}}(r) = \frac{\Delta f(r)}{S_k} \tag{2.3.2}$$

where S_k is the speed of k-space traversal, i.e.,

$$S_k = \frac{\Delta k_{\mathrm{PE}}}{\Delta t_{\mathrm{PE}}} = \frac{N_{\mathrm{int}}\, R}{\mathrm{FOV}_{\mathrm{PE}}\, T_{\mathrm{ESP}}} \tag{2.3.3}$$

Here, Δk_{PE} is the distance between adjacent k-space lines during readout, and Δt_{PE} is the time interval between the echoes from these k-space lines, which is equal to the echo spacing, T_{ESP}.

As seen in Eqn (2.3.2), one can reduce susceptibility artifacts by reducing the *off-resonance effect*, or $\Delta f(r)$. This goal can be achieved to a certain extent by passive or active shimming of the areas of interest (see Section 2.3.3.6 and Chapter 2.2); however, local field inhomogeneities remain unaddressed.

The other (rather more tortuous) method is to *accelerate the traversal of k-space* (i.e., increase S_k) by altering the MRI pulse sequence, as outlined schematically in Figure 2.3.3. A reduction of the *echo spacing* (T_{ESP}) can be achieved by (1) increasing the EPI bandwidth and/or sampling on the gradient ramps of the EPI trajectory, and/or (2) segmenting the k-space trajectory, such as by the readout-segmented EPI approach (a "multishot" method). Interleaved EPI methods speed up the k-space traversal by dividing the k-space into several sections that are each acquired faster but in separate repetition times (TRs).[6–8] A reduction in the *phase-encoding* FOV ($\mathrm{FOV}_{\mathrm{PE}}$) in spine imaging with standard slice-selective pulses can cause undesired aliasing in the PE direction if the object is larger than $\mathrm{FOV}_{\mathrm{PE}}$, even after using graphical saturation pulses. Thus, more advanced reduced FOV methods that alter the radiofrequency (RF) pulses or that use outer volume suppression methods have been implemented for the spinal cord.[9–12] Parallel imaging methods provide *acceleration* in k-space by utilizing the complementary spatial encoding information from multiple receiver coil elements to reduce the number of acquired k-space lines.[13–15]

Ideally, a combination of all of these methods could be used; however, each of these techniques presents a rather complicated set of advantages and limitations.

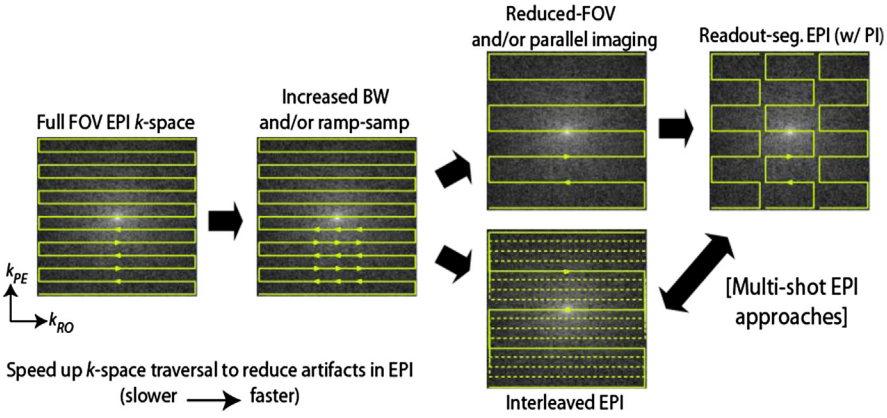

FIGURE 2.3.3 Overview of some of the MRI pulse sequence techniques described in this chapter. To reduce susceptibility artifacts in EPI, we need to speed up *k*-space traversal (methods are listed in increasing k-space traversal speed, with faster methods on the right). Increased readout bandwidth (BW) and ramp sampling both help decrease the echo spacing between adjacent *k*-space lines. Reducing the phase-encoding FOV, parallel imaging, and dividing the *k*-space into interleaves all help to speed up *k*-space traversal by skipping lines during readout in a single TR. A more advanced multishot method is to segment the *k*-space along the readout direction to shorten the echo spacing. These methods can be combined to reach a desired level of acceleration.

The remainder of this section discusses various approaches to reduce susceptibility distortions, and their relative advantages and disadvantages.

2.3.3.1 Reduced Echo-Spacing Methods

Susceptibility effects can be alleviated by reducing the echo spacing between adjacent *k*-space lines during readout in a single TR. For a fixed image resolution, the easiest way to achieve this goal is (1) to increase the readout bandwidth (BW), and/or (2) to acquire data during the gradient ramps (also known as "ramp sampling") in addition to the gradient plateaus. Increasing the bandwidth reduces the signal-to-noise ratio (SNR) due to a shorter readout. However, if a region experiences severe off-resonance effects, the decreased readout duration can actually reduce the dephasing in a voxel, resulting in an *increase* in local signal level. Ramp sampling is an especially important implementation that comes at very little disadvantage, other than the need for 1D-gridding of the data acquired during gradient ramps.

Both ramp sampling and increasing the bandwidth are methods available on most commercial MRI scanners. In some scanners, there is no direct relationship between the echo spacing and the BW, due to hardware limitations (e.g., gradient-switching time). In practice, the user can increase the BW and stop when the echo spacing is at its minimum. Note that although reducing the echo spacing is the easiest way to alleviate susceptibility artifacts, it can fail to provide a significant improvement in image quality, given that the readout bandwidth in an MRI scanner has an upper limit (typically a maximum of ±250 kHz). The methods described in the remainder of this section usually build on top of a ramp-sampled, high-bandwidth EPI sequence, and they provide additional ways to speed up *k*-space traversal in EPI.

2.3.3.2 Reduced Field-of-View Methods

Spinal cord imaging has been shown to benefit from reduced FOV (rFOV) acquisitions that limit the extent of coverage in the phase-encoding direction (i.e., FOV_{PE}). With a much smaller FOV_{PE}, the number of required *k*-space lines is also reduced (typically between one-half and one-fourth of the full-FOV case), which in turn significantly reduces off-resonance induced artifacts. As expected, the SNR is also reduced by the square root of the FOV_{PE} reduction factor. Although both reduced-FOV and parallel imaging methods reduce the number of acquired *k*-space lines to achieve high-quality images, they significantly differ in implementation. Parallel imaging methods (see Section 2.3.3.3) take advantage of the orthogonality of coil sensitivities, while the rFOV techniques actively limit the extent of FOV through pulse sequence modifications.

Figure 2.3.4 demonstrates the effectiveness of rFOV techniques, where reducing the FOV_{PE} to one-fourth of its full-FOV value alleviates the distortions in the ss-EPI image of the spinal cord, even in the presence of metallic implants.[16] Recently, a number of rFOV methods have been proposed for high-resolution ss-EPI of the spinal cord. A schematic explanation of some of these methods is given in Figure 2.3.5.

One of these rFOV methods utilizes outer-volume suppression pulses preceding the excitation pulse[10] (shown in Figure 2.3.5(A)). This technique can be implemented by placing suppression bands anterior and/or posterior to the spine. Similar implementations of this

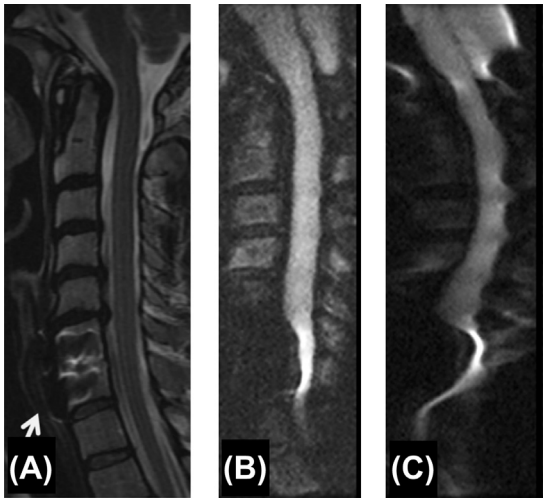

FIGURE 2.3.4 Diffusion-weighted ss-EPI images of the cervical spine of a patient post cervical discectomy and fusion, acquired using a four-channel spine array coil with phase encoding performed in the anterior–posterior direction, and matrix size = 192 × 192. (A) T_2-weighted fast spin-echo image is given for anatomical reference. ss-EPI images with (B) a 25% FOV_{PE} (i.e., 18 cm × 4.5 cm), and (C) full FOV (i.e., 18 cm × 18 cm). The reduced-FOV image (B) has fourfold reduced distortion when compared to the full-FOV image (C), demonstrating the effectiveness of the reduced-FOV method in alleviating susceptibility-induced distortions. Note that the reduced-FOV method mitigates but does not fully eliminate the metallic artifact associated with the plate between the vertebral bodies. *Source: Figure from Ref. 16.*

method are available on most commercial MRI scanners, and they usually involve graphical prescription of suppression and saturation bands. However, because the suppression efficiency is generally limited, it can lead to partial aliasing artifacts in the PE direction of the images. These artifacts are sometimes difficult to detect, as the aliased signal can resemble noise due to its attenuated amplitude. Hence, it is imperative to perform phantom tests to assess the level of signal suppression outside the desired FOV_{PE}.

Another rFOV technique applies excitation and refocusing RF pulses orthogonally[17] (see Figure 2.3.5(B)), which significantly decreases the SNR of the neighboring slices if interleaved acquisition is performed. This is because the 180° pulse acts as an inversion pulse on the neighboring slice locations. A method called ZOOM-EPI[9] mitigates the SNR loss problem by applying the 180° refocusing pulse at an oblique angle, as shown in Figure 2.3.5(C). This way, the neighboring slices do not experience the refocusing pulse. However, if the neighboring slices are close to each other in space, there can still be a partial cross-saturation of the adjacent slices, resulting in a signal drop along the edges of the FOV in the PE direction. This signal drop can be alleviated by spacing the slices apart (i.e., by placing slice skips) or by extending FOV_{PE}. A recent approach called contiguous-slice zonally oblique multislice (CO-ZOOM) mitigates the cross-saturation problem by double refocusing the signal with two 180° pulses applied orthogonally as in Figure 2.3.5(B).[12] However, the resulting prolonged echo time (TE) decreases the signal level.

Instead of utilizing a 1D excitation pulse, 2D spatially selective RF pulses can be used to excite only the ROI for rFOV imaging.[11,18] As shown in Figure 2.3.5(D), because the adjacent slices are not excited, this method is compatible with contiguous multislice imaging without the need for a slice skip. Depending on the implementation, these 2D-RF pulses have excitation profiles periodic in either the phase or the slice direction. A subsequent 180° refocusing pulse can be utilized to refocus only the main lobe of the excitation while preserving the rFOV imaging capabilities,

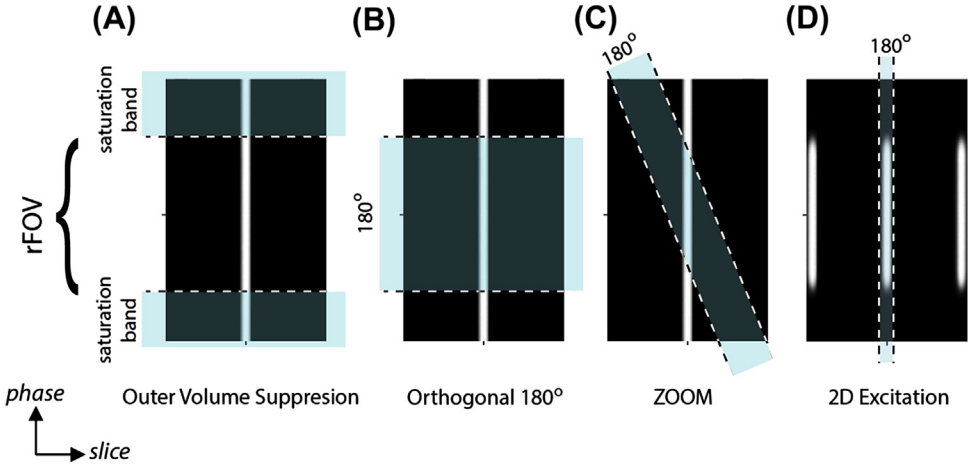

FIGURE 2.3.5 Schematic explanation of various reduced-FOV imaging methods. (A) Outer volume suppression and saturation methods utilize a regular 90° excitation followed by two suppression bands placed anterior and posterior to the region of interest. (B) Regular 90° excitation followed by an orthogonally applied 180° refocusing pulse. The 180° pulse inverts the adjacent slices, reducing the SNR during imaging. (C) ZOOM-EPI method with a tilted 180° refocusing pulse. (D) 2D spatial excitation, followed by a 180° refocusing pulse.

as demonstrated in Figure 2.3.5(D).[11] When the profile is periodic in the slice direction, the fat and water profiles are also shifted in volume in the slice direction. This feature can be exploited by designing a 2D-RF pulse with nonoverlapping fat–water profiles. Then, the subsequent 180° refocusing pulse suppresses the signal from fat without the need for additional fat suppression pulses. However, the periodicity in the slice direction may also restrict the coverage in the slice direction.[11] Likewise, if the excitation profile is periodic in the phase direction, it may place a restriction on the maximum size of the subject. This is because the periodic lobes in the phase direction can otherwise cause aliasing artifacts, as those lobes are now refocused with the 180° pulse.[18] Furthermore, because the 2D-RF pulses tend to have long durations, the slice profiles may be sensitive to off-resonance effects.

Each of these rFOV methods has its own strengths and weaknesses, and the method of choice depends on the application. In the end, they all significantly reduce the susceptibility-induced artifacts in EPI.

2.3.3.3 Parallel Imaging

Parallel imaging helps reduce the effective readout duration by decreasing the number of *k*-space lines (see Chapter 2.1). Data from multiple channels are then used to fill in the "missing" *k*-space lines through parallel imaging reconstruction procedures (such as GRAPPA[19]) or unalias reconstructed images (using SENSE[20]). Since a fully sampled *k*-space data set can be reconstructed from the undersampled *k-space* acquired in one repetition, parallel imaging–enhanced EPI is relatively robust to motion artifacts.

While parallel imaging is frequently used for distortion reduction in EPI brain scans, its efficacy is limited by both the number of available receiver coils and their geometric arrangement. This is particularly the case for spine array coils, which are often geometrically flat, have poor sensitivity in the anterior–posterior (A/P) direction, and have limited parallel imaging capability in the S/I direction. Figure 2.3.6 compares cervical spine images acquired both with and without parallel imaging performed in the A/P (phase-encoding (PE)) direction. Figure 2.3.6(C) and 2.3.6(D) were acquired with the same scan time as in Figure 2.3.6(B), but with acceleration factors of $R = 2$ and $R = 3$, respectively. While accelerating through *k*-space results in a two- or threefold reduction in distortion, the overall SNR is reduced for a given scan time. Even though the scan times were adjusted so that the accelerated images had approximately the same number of samples as in the unaccelerated image, one can observe the *g*-factor noise that obscures the pons region. This is more pronounced for the image with

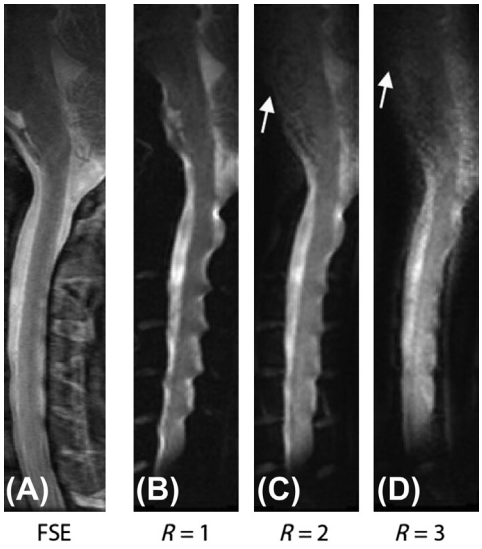

FIGURE 2.3.6 Cervical spine images acquired using a four-channel spine array coil using a matrix size = 192 × 192 and a FOV = 18 cm × 9 cm (with PE performed in the A/P direction). (A) T_2-weighted fast spin-echo image is given for anatomical reference. Standard ss-EPI with (B) no acceleration, (C) $R = 2$ giving a twofold reduction in geometric distortion, and (D) $R = 3$ giving a threefold reduction in geometric distortion. All images have the same scan time. Because of the shorter trajectory and g-factor noise present in (C–D), the SNR is reduced overall. Especially the pons area experiences a significant SNR reduction, due to the diminishing coil sensitivity profiles in the A/P direction (white arrow). The decreased image quality with $R = 3$ suggests that $R = 2$ is probably the upper acceleration limit for this spine array coil.

$R = 3$, but it is noticeable even with a modest parallel acceleration factor of $R = 2$. It is for this reason that many studies of the spinal cord utilizing parallel imaging to reduce susceptibility artifacts in EPI only achieve a factor of (or near) 2.[13–15,21] At such small acceleration factors, parallel imaging alone is often not effective in obtaining submillimeter in-plane resolution with adequate image quality.

For cervical scans, one may be inclined to use a head and neck array coil in order to leverage on its improved parallel imaging performance capability. Unfortunately, few conventional head and neck coils have geometric arrangements suitable for high acceleration factors. However, some promising work has been shown with the development of a 32-channel coil that fully covers the brain and cervical spine.[22] Diffusion tensor imaging (DTI) results acquired with this coil are shown in Figure 2.3.7, with noticeable reduction in geometric distortion with increasing acceleration factors (of up to four).

2.3.3.4 Multishot EPI Techniques

As shown in Figure 2.3.3, it is possible to reduce susceptibility artifacts by traversing *k*-space faster through the use of multishot EPI techniques. The most common

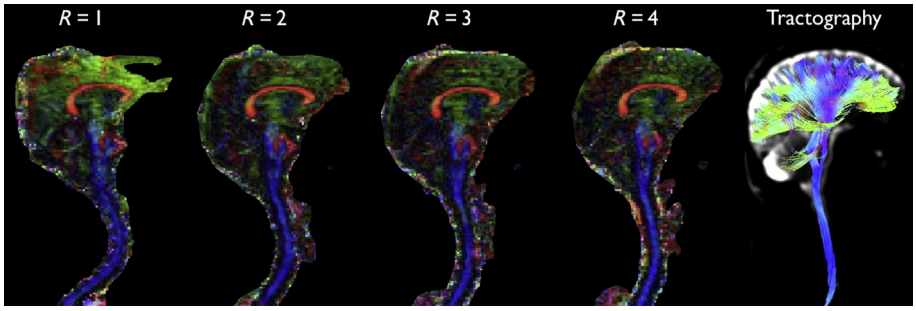

FIGURE 2.3.7 Parallel imaging at various acceleration factors using EPI readout and a 32-channel coil that fully covers the brain and cervical spine.[22] Fractional anisotropy (FA) color maps from this DTI scan show a noticeable reduction in geometric distortion with increasing acceleration factors. GRAPPA reconstruction was utilized for parallel imaging. TR = 14280 ms, echo time (TE) = 80 ms, resolution = $1.7 \times 1.7 \times 1.7$ mm^3, 30 diffusion-encoding directions, b-value = 800 s/mm^2. *Source: Images courtesy of Julien Cohen-Adad.*

multishot EPI technique is called interleaved EPI (IEPI),[23] which is becoming a promising approach in clinical spine DWI acquisitions.[6–8,24–28] With this method, the number of k-space lines per interleaf is reduced by acquiring multiple EPI interleaves in the phase-encoding direction. For example, for $N_{int} = 2$, each interleaf traverses the k-space by skipping every other line. These two interleaves are then combined to form the full k-space data. The disadvantage of the IEPI approach is that motion can occur between the acquisition of different interleaves, which can lead to ghosting artifacts or even result in gaps in k-space (for diffusion-MRI methods after phase correction), leading to aliasing artifacts and residual ghosting in the final image.

Figure 2.3.8 demonstrates that one can acquire anatomically reliable DWI images using IEPI with 11 shots (and 15 echoes per interleaf). According to Eqn (2.3.1), the distortion artifacts can be reduced by a factor that is proportional to the number of interleaves. The shortened readout in IEPI helps to reduce image blurring that is caused by field inhomogeneity and chemical shift. In addition, the flexibility in choice of interleaves in IEPI allows one to use larger acquisition matrices, which enables one to acquire images with higher spatial resolution. With smaller voxel sizes, distortions from intravoxel dephasing can also be mitigated. Multiple signal averages (excitations) can then be used to compensate for the decreased SNR associated with smaller voxels. Some work has coupled the IEPI approach with reduced FOV for DWI, achieving images at a resolution capable of revealing strong diffusional anisotropy in spinal cord white matter.[28]

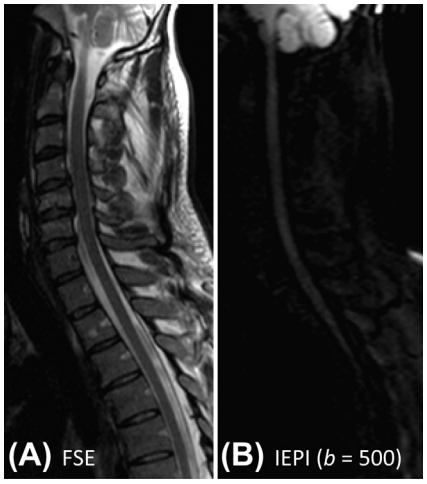

FIGURE 2.3.8 Isotropic diffusion-weighted interleaved EPI sequence showing high geometric fidelity in the spinal cord. (A) T_2-weighted fast spin-echo image for anatomical reference, and (B) isotropic diffusion-weighted image acquired using IEPI (15 lines and 11 shots), with b-value = 500 s/mm^2.

The trade-off for using a multishot echo planar technique is that the segmentation of k-space not only increases the scan time compared with single-shot EPI but also results in phase error discontinuities from off-resonant spins and random motion-induced phase fluctuations for each interleaf.[29] Phase error discontinuities require echo-time shifting,[29] as well as monitoring and retrospective correction of phase errors by means of navigator echoes.[30,31]

Despite the use of navigators in IEPI, motion remains a difficult problem, particularly for diffusion imaging where significant motion can cause gaps in between the interleaves, resulting in aliasing artifacts. An alternative multishot approach that is less prone to motion is readout-segmented EPI (RS-EPI),[32] which covers k-space with a series of consecutive segments. As in Eqn (2.3.1), in RS-EPI the echo-spacing T_{ESP} is reduced by segmenting the k-space trajectory along the readout dimension. Here, geometric distortion is reduced by an extent that is roughly inversely proportional to the width of the segment. In RS-EPI, each segment acquires a full-FOV (low-resolution) image that is largely motion-free. Thus, correction for motion is required

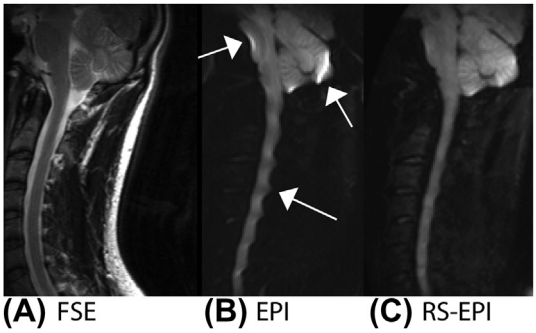

FIGURE 2.3.9 Cervical spine images showing (A) a fast spin-echo for geometric reference, and isotropic diffusion-weighted ($b = 500$ s/mm^2) images acquired at matched resolution (1.5 mm × 1.5 mm × 4 mm) and matched scan time (2:30 min) using (B) EPI (echo spacing = 726 μs) and (C) RS-EPI (effective echo spacing = 316 μs).

only between segments, which can be performed with the use of a navigator image. Any "gaps" in *k*-space that arise due to this correction are quite benign as demonstrated in DWI neuroimaging.[33] Figure 2.3.9 shows a comparison between EPI and RS-EPI isotropic diffusion-weighted images acquired with the same scan time at a matrix size of 192 × 192. Using 32 × 192 segments in RS-EPI results in a 2.3-fold reduction in distortion. It is possible to further reduce susceptibility artifacts using smaller segment widths, which is analogous to the use of more interleaves in IEPI. However, this comes at a considerable cost in SNR efficiency and greater sensitivity to motion artifacts.

As in reduced-FOV IEPI, it is intuitive to use RS-EPI with reduced-FOV imaging approaches to get the benefits of both methods for reducing distortion. Figure 2.3.10 shows the improvement of image quality in a thoracic DTI scan as one goes from standard (full FOV) EPI, to reduced-FOV ZOOM-EPI, and finally to reduced-FOV ZOOM-RS-EPI.

In addition, equipped with a coil suitable for parallel imaging, one can also benefit from accelerating the RS-EPI trajectory with parallel imaging. As shown in

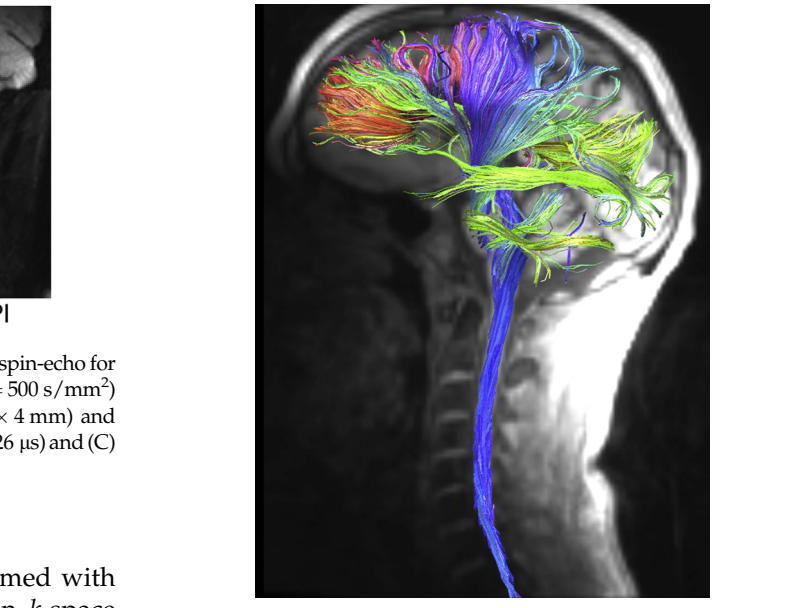

FIGURE 2.3.11 Fiber tractography using parallel imaging combined with RS-EPI. This image was acquired using a 32-channel brain and spine coil,[22] 3 RS-EPI segments, 34 slices, cardiac gating, 2.2 mm isotropic resolution, TR/TE = 15 s/66 ms, matrix=138 × 104, $R = 3$ (GRAPPA reconstruction), BW = 1510 Hz/pixel, echo spacing = 0.38 ms, twice-refocused pulse, b-value = 800 s/mm^2, 30 diffusion-encoding directions. *Source: Images courtesy of Julien Cohen-Adad.*

Figure 2.3.11, it is possible to achieve high-quality fiber tractography images of the cervical spinal cord and brain with the use of RS-EPI accelerated by a factor of 3.

2.3.3.5 Other (Non-EPI) Techniques

2.3.3.5.1 Line Scan Imaging

Line scan imaging is an alternative to the EPI acquisition scheme that has been used for diffusion-weighted MRI in the spinal cord. It consists of sequential single-shot acquisition of PE lines. Line scan imaging is relatively insensitive to B_0-field inhomogeneities, eddy currents, and bulk motion, and can provide rectangular

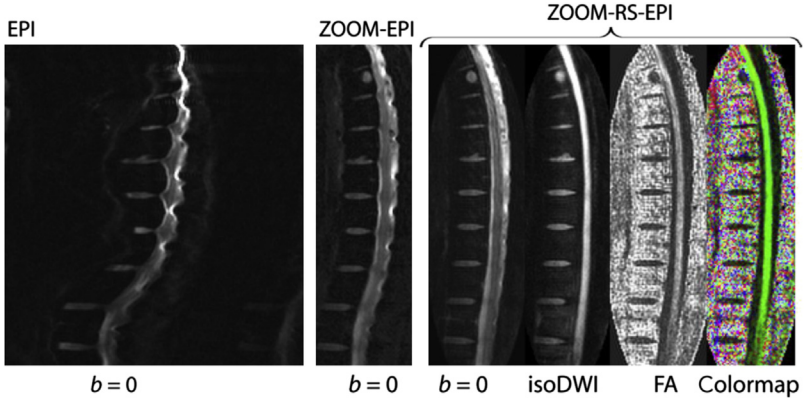

FIGURE 2.3.10 Comparison between the $b = 0$ s/mm^2 images of a thoracic spine using full FOV EPI (30 × 30 cm, matrix size = 200 × 200), ZOOM-EPI, and ZOOM-RS-EPI (30 × 10 cm, matrix size = 200 × 60 (square pixels)). For ZOOM-RS-EPI, the isotropic DWI (isoDWI, $b = 500$ s/mm^2), fractional anisotropy (FA), and the first eigenvector (color map) are also shown. Note that there is less "disc bulging" into the spinal canal and less blurring on the ZOOM-RS-EPI scans than on the ZOOM-EPI scans.

diffusion-weighted images.[34–36] Previous studies have compared single-shot EPI and line scan imaging.[37] It was applied in children,[38] in the human spinal cord,[39–41] and in the spine.[42] However, the trade-off of line scan imaging acquisition schemes is the relatively long acquisition time to image a large volume, and missing k-space lines in the presence of extensive motion.

2.3.3.5.2 Fast Spin-Echo

Rapid acquisition with relaxation enhancement (RARE) is a spin-echo (SE) sequence with refocusing pulses after RF excitation to significantly decrease relaxation time, thus enabling the introduction of more excitation pulses in a given time in comparison to the standard SE sequence. With RARE, the RF refocusing yields signal decay with T_2 rather than T_2^*, making this sequence less sensitive to off-resonance effects and eddy currents.[43] A number of variations of the RARE sequence have been developed, including fast spin-echo (FSE) and turbo spin echo (TSE). Some studies have demonstrated the benefits of FSE for imaging the human spinal cord with DTI.[13,44,45] Although faster than standard SE, this sequence is much slower than EPI.

2.3.3.5.3 Radial and Spiral Acquisition

In contrast to the classical Cartesian *k*-space filling, radial acquisition is made up of phase lines passing through the center of *k*-space, while spiral acquisition consists of acquisition in a "spiral" trajectory starting from either the center or periphery of *k*-space. Hence, in both radial acquisition and spiral acquisition, all readout trajectories are symmetric to the origin of k-space and are equivalent with respect to the reconstruction. This is not the case in conventional Cartesian readout schemes, where a single corrupted data line can degrade the complete image.[46] Due to the high density of data at the center of *k*-space, the SNR is still acceptable when fewer phase lines are acquired compared to the Cartesian *k*-space sampling scheme. A disadvantage of radial and spiral acquisition schemes, however, is the potential for streak or "aura" (or swirl) artifacts due to the undersampling of the azimuthal regions in *k*-space.[47] Instead of single lines, one could acquire blades consisting of several lines, which are then rotated to provide better navigation capabilities.[48,49] This technique is known as periodically rotated overlapping parallel lines with enhanced reconstruction (PROPELLER). A radial EPI technique using this approach has been proposed and yielded very promising results in the abdomen[50] and in the spinal cord.[51] Here, it is important to note that for the EPI-variant of PROPELLER, the readout is along the short axis of the blade to shorten the echo spacing. The radial FSE technique was further improved by using a wider refocusing slice to decrease B_1-field inhomogeneity effects.[52,53] Additionally, self-navigated, interleaved, variable-density spiral-based DTI acquisition (SNAILS) at high spatial resolutions have recently shown promising results in a cat model of spinal cord injury during free breathing.[54]

2.3.3.6 Decreasing Off-Resonance

In addition to adjusting the imaging parameters, susceptibility artifacts can be reduced by repositioning the subject, reorienting the slice, or applying active- and/or passive-shimming methods. For example, the curvature in the neck creates an abundance of air–tissue interfaces, and the resulting magnetic field inhomogeneity makes fat suppression difficult. To improve the magnetic field homogeneity, the patient's head can be supported by foam pads in order to achieve maximum anteflexion without the patient feeling uncomfortable.[8] In this position, the neck rests nearly flat on the coil, minimizing the volume of air between the spine and the coil. This repositioning makes the subsequent shimming more effective, especially when using surface coils. In kyphotic patients, however, this can be rather difficult to perform. For axial imaging of the spine, instead of repositioning the patient, one can carefully reorient the slices so that they are centered within vertebral bodies.[55] This in turn minimizes the effects of field inhomogeneities from vertebral bodies shown in Figure 2.3.1(B).

Off-resonance artifacts can also be improved by active or passive shimming of the ROI. Of the active-shimming methods, first-order gradient shimming of the ROI is standard in most MRI scanners. These shims only correct for linear variations in the local field. However, spinal cord imaging can significantly benefit from higher order shimming, especially at high field strengths. As seen in Figure 2.3.12(A), both the signal level and the distortion (seen with the curvature of the spine) are improved by applying a second-order shim.

Another way to improve field homogeneity near the air-tissue interface is to fill the air with a material that is susceptibility-matched to tissue to move the inhomogeneities outside the imaging FOV. This is a simple, passive, and direct technique for reducing B_0 inhomogeneities at air-tissue boundaries. For this method to be effective, the susceptibility-matching material needs to be MRI invisible, such that it does not extend the size of the FOV in any direction. These criteria are satisfied by fluids such as perfluorocarbon,[56] barium sulfate-doped water,[57] Kaopectate,[58] and a recently proposed pyrolytic graphite (PG)-doped foam.[59] Figure 2.3.12(A) demonstrates how this PG foam improves the field map around the spine when it is positioned behind the neck.

Although active- and passive-shimming methods can significantly improve the image quality, they both have

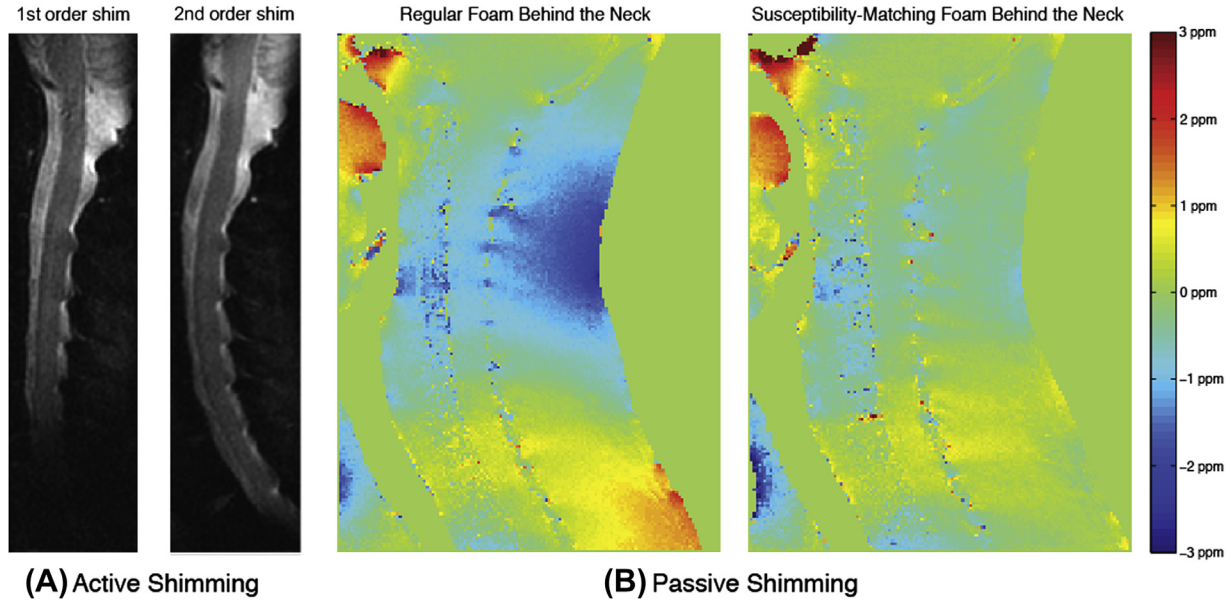

FIGURE 2.3.12 Effects of shimming on susceptibility-induced off-resonance. (A) T_2-weighted reduced-FOV ss-EPI images of the spinal cord, acquired at 3 T, with first-order (i.e., linear) shim versus second-order shim. Note the improvement in the signal level and distortion (seen with the curvature of the spine) using higher order shimming. (B) Field maps of the spine acquired with regular foam versus susceptibility-matching foam placed behind the neck. With the susceptibility-matching foam, the air volume in the back of the neck is filled with a material that has the same magnetic susceptibility as that of human tissue. Hence, the field map is significantly improved *(Source: Passive-shimming images courtesy of Gary Lee)*. Please see Chapter 2.2 for more information on shimming.

limitations. Active-shimming methods cannot correct for high-spatial-frequency perturbations in the field,[60] because the shim coils are physically too large to generate high-spatial-frequency field patterns deep within a patient.[1] Similarly, passive-shimming methods can only fix the problems where the air–tissue interface is accessible, and they cannot address susceptibility variations due to air in the lungs, trachea, and sinuses. In addition, some of the shimming methods are difficult to apply in clinical settings. Hence, it is best to combine practical shimming methods with acquisition- and reconstruction-based distortion reduction methods, some of which are discussed in Section 2.3.3.7.

2.3.3.7 Distortion Correction Methods

While distortion correction methods have been used for neuroimaging applications for quite some time, there are a few studies that have incorporated and tailored the use of these methods for spinal cord imaging. It is not surprising that these postprocessing methods are not readily available on clinical MRI scanners.

There are a number of "distortion correction" strategies available, including the point spread function (PSF),[61] phase field map method,[62–64] reversed gradient polarity method (RGPM),[65–69] and co-registration methods.[70,71] The first three of these methods must incorporate extra measurements in the acquisition, and all of these methods require extra postprocessing steps.

In the *phase field map* method, a B_0 field map is acquired for each subject and then used to undistort the accompanying EPI data.[62–64] This method is widely used (e.g., it is implemented in FSL[b], a comprehensive library of analysis tools for fMRI). The standard procedure consists of (1) acquiring two gradient echo images at different TEs, then subtracting the phase data to obtain the phase field map (also see Chapter 2.2); (2) processing it to generate a warping matrix; and (3) applying this warping matrix to EPI series. For regions particularly prone to inhomogeneities (e.g., close to the lungs),[72] phase field maps may exceed 2π, therefore producing "phase wraps". To correct for these phase wraps, one could use automatic algorithms that identify phase discontinuities based on a standard intensity segmentation, and then correct phase errors at wrap interfaces.[73] Acquisition of a more accurate B_0 field map (in comparison with the standard double echo technique) can provide improvement to the phase field map technique in the spinal cord. For example, acquiring more than two echoes could provide a way to unwrap phase maps on a voxel-by-voxel basis.

The *point spread function* (PSF) mapping method uses a separate reference scan that introduces an additional distortion-free dimension in *k*-space that can be

[b] http://www.fmrib.ox.ac.uk/fsl/fugue/index.html.

Fourier-transformed into the PSF for each voxel. These images provide additional information about distortions in all directions, as well as the intensity distribution for each voxel. By considering the displacement of the PSF, local distortions due to susceptibility and chemical shift effects can be quantified and subsequently corrected. This technique can be combined with other acquisition methods for faster imaging, such as parallel imaging. The PSF method has been shown to reduce artifacts around the intervertebral disks and provide better consistency of fiber tractography compared with uncorrected images.[74] However, a disadvantage of this approach is that the correction is performed in *k*-space, which can be problematic for diffusion MRI data due to the large phase shifts introduced by diffusion encoding.[75]

The RGPM or "blip-up blip-down" method uses an additional EPI volume acquired with the same FOV and matrix, but using a reversed PE direction (i.e., it is rotated 180°). Reversing the PE results in a sign reversal of $\Delta f(r)$ in Eqn (2.3.1). As a result, images acquired with reversed gradients exhibit distortions in the opposite direction. Using images acquired with both the positive and the negative phase gradients, geometric and intensity correction fields are estimated and subsequently applied to EPI data sets. In DTI, the same deformation field can be applied to all diffusion-weighted data after motion correction. Since this method does not involve extensive calibration measurements like in the case of the PSF mapping method, nor does it rely on measured field maps, it is relatively practical to use with minimal scan time increase. Figure 2.3.13 shows EPI images acquired with opposite PE gradients, with subsequent correction using the phase map estimated from the difference between these two images.

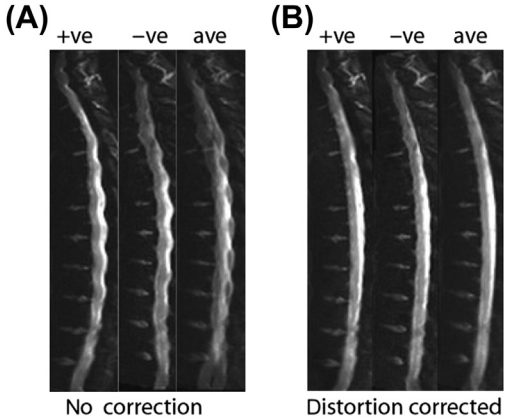

FIGURE 2.3.13 Distortion correction using the reversed gradient polarity method (RGPM). (A) T_2-weighted images of the thoracic spine acquired with a positive (+ve) and negative (−ve) phase-encoding gradient, and the average of the two images (ave). (B) Distortion-corrected images produced by using the displacement map calculated from the +ve and −ve images. A substantial improvement of image quality can be seen, particularly when the +ve and −ve images are averaged.

For *co-registration methods*, geometric distortion is corrected using nonlinear registration procedures, by warping distorted EPI images onto a corresponding undistorted (anatomical) reference image, so that their global shape would tend to be similar to their theoretical undistorted one.[71] The reference image is typically a T_2-weighted FSE sequence, acquired with the same FOV as the EPI image. The method consists of (1) manually segmenting the ROI to optimize the registration procedure, (2) normalizing intensity histograms for both EPI and FSE images, and (3) estimating a slice-dependent nonrigid deformation field constrained in the PE direction. This method is advantageous because no additional volume acquisition is required, except a reference image without distortion, which is incidentally generally acquired by default in standard protocols. However, the task of eliminating distortions in this way can be difficult, as the contrast between the reference and EPI image is often quite different, and the transformation has considerably more degrees of freedom than a simple rigid-body transform.[75] This method has been shown in fMRI brain data to provide improved matching between anatomical and functional MRI data; however, it does not fully remove the geometrical distortions since it does not rely on an accurate measure of these distortions.[71]

In all of the methods discussed here, intensity errors can also be corrected using the geometric displacement map. For example, if two voxels are stretched, the intensity in each voxel will be reduced. Similarly, if two voxels are squeezed, their intensity will be increased. Intensity correction will therefore multiply each distortion-corrected voxel by a correcting factor to compensate for intensity error. It should be noted that while voxels that are stretched due to distortion can be restored, the spatial details of the voxels that are bunched up cannot be recovered (these voxels will only be spread across a voxel range after correction). Note that the fidelity of all distortion correction methods relies on a reasonable image quality. That is, if the underlying image is overly distorted, the methods result in an inaccurate measurement of the displacement field and in lost anatomical information.

2.3.4 COMPARISON OF METHODS TO REDUCE SUSCEPTIBILITY ARTIFACTS

A basic summary of the methods that reduce susceptibility artifacts in EPI, and their relative advantages and disadvantages, are given in Box 2.3.1. To demonstrate the improvements in susceptibility artifacts achieved

BOX 2.3.1

BASIC SUMMARY OF METHODS THAT REDUCE SUSCEPTIBILITY ARTIFACTS IN EPI, AND THEIR RELATIVE ADVANTAGES AND DISADVANTAGES

Method	Target Parameter	Pros	Cons	Difficulty (*Easiest and ***Hardest)
Increased BW	T_{ESP}	• Simple and effective	• Limited by gradient and BW specs	*Available on most scanners
Ramp sampling	T_{ESP}	• Simple • Improved signal-to-noise ratio (SNR)	• Provides minor improvement	*Available on most scanners
Reduced FOV	FOV_{PE}	• Significant reduction in distortion level • A variety of methods to choose from	• May require modifications to RF pulses • May reduce SNR and/or affect slice coverage (depending on method of choice)	**Available on some scanners
Parallel imaging	R	• Can be combined with other methods (e.g., with reduced-FOV methods)	• Requires suitable phased-array coils—typically allows only $R \leq 2$ in A/P direction in spine • May cause spatially correlated noise	**
Interleaved EPI (IEPI)	N_{int}	• Flexibility to choose number of interleaves based on desired distortion reduction	• Increased temporal footprint • Increased scan time • Prone to motion between interleaves • May require navigator echoes and tailored reconstruction	***
Readout-segmented (RS)-EPI	T_{ESP}	*Compared with IEPI* • More effective motion correction • In DWI, much improved data consistency and fewer "gaps" in *k*-space	• Increased temporal footprint • Prone to motion between segments—requires tailored reconstruction for motion correction and gridding *Compared with IEPI* • Inefficient use of gradients reduce SNR • Reduction in distortion through selection of segment width limited	***
Shimming	$\Delta f(r)$	• Also improves signal level and fat suppression	• Only fixes large-scale off-resonance effects	**Available on most scanners
Distortion correction methods (postprocessing)		• Effective in correcting residual distortions • Data used for distortion correction can be used to boost SNR (for RGPM)	• Requires additional postprocessing • Increases scan time (for most approaches) • Not effective if original images are overly distorted	***

Note that compared with standard EPI, all of these approaches (excluding ramp sampling, shimming, and distortion correction) to varying degrees come at a reduced SNR efficiency.

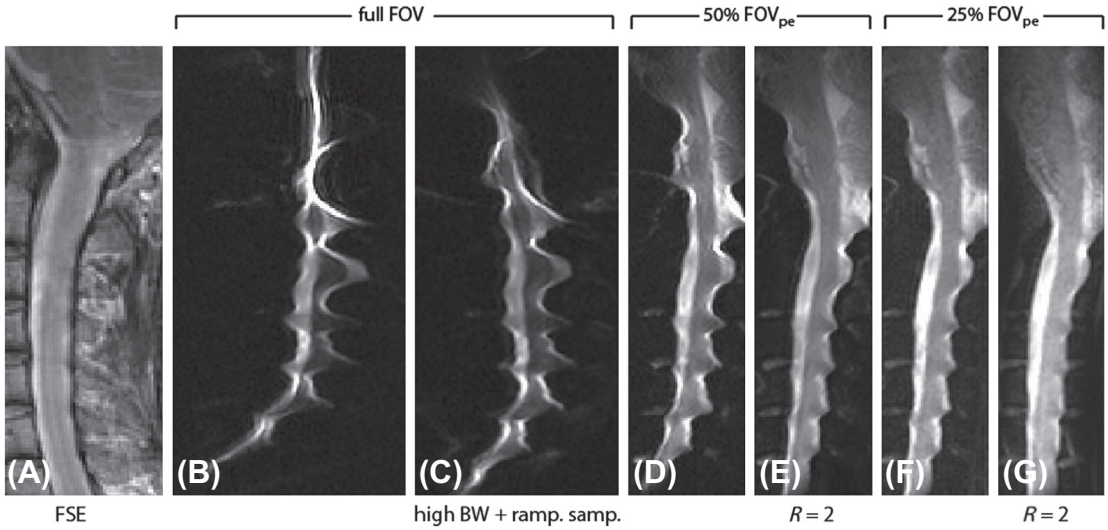

FIGURE 2.3.14 Comparison of some of the acquisition-based methods to reduce susceptibility artifacts. T_2-weighted EPI images of the cervical spine were acquired with a high in-plane resolution of 0.94 mm × 0.94 mm (corresponding to a 192 × 192 matrix size for full-FOV images), using a four-channel spine array coil at 3 T. The scan time was kept constant for all methods. (A) Fast spin echo (FSE) image showing anatomical reference. (B–C) Full FOV (18 cm × 18 cm) images, where (B) is acquired without ramp sampling, and (C) with ramp sampling and higher bandwidth (BW). Although these two simple changes help reduce the geometric distortion (see the difference in the curvature of the spine between (B) and (C)), the image quality is still not good. Reducing the FOV, on the other hand, significantly helps with the image quality. (D–E) 50% FOV_{PE} (i.e., 18 cm × 9 cm) images; and (F–G) 25% FOV_{PE} (i.e., 18 cm × 4.5 cm) images. Note that (E) and (B) also incorporate a parallel acceleration factor (R) of 2, with (G) displaying the best overall image quality among the compared images. While (E) and (F) have roughly the same geometric distortion properties, (E) shows some parallel imaging–induced noise in the pons.

via some of the methods presented in this chapter, in vivo T_2-weighted EPI of the cervical spinal cord was performed on a healthy subject, with the results shown in Figure 2.3.14. An FSE image is included for anatomical reference. The regular (i.e., "full-FOV") EPI images exhibit very high levels of distortion. The spinal cord has a comb-like appearance due to susceptibility differences between the cord, CSF, and vertebral bodies. The cord appears to have an unnatural convex curvature, instead of its concave shape as given in the anatomical reference in Figure 2.3.14(A). These artifacts are only slightly alleviated by ramp sampling at a higher BW. Reducing the FOV, however, significantly helps with the distortions and signal dropouts. A combination of reduced-FOV imaging and parallel imaging achieves the best overall image quality in this comparison. Further improvements in image quality can be achieved via the distortion correction methods mentioned in Section 2.3.3.7.

Combining distortion correction techniques with acquisition-based methods can further improve the quality of resulting images. Figure 2.3.15 shows such an example where thoracic spine images were produced using a combination of three of the methods mentioned in this chapter: reduced FOV imaging, the RS-EPI trajectory, and RGPM distortion correction. The combination of these methods (Figure 2.3.15(D)) provides an image that anatomically closely matches the undistorted FSE image (Figure 2.3.15(A)).

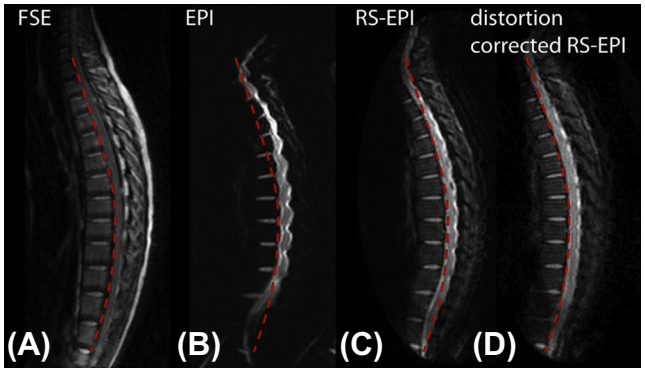

FIGURE 2.3.15 T_2-weighted thoracic spine images showing a comparison between (B) EPI and (C) readout-segmented (RS)-EPI. In (D), the RS-EPI image has been distortion corrected with the use of a $b = 0$ image acquired with a negative phase-encoding gradient, helping to remove some of the residual distortion inherent in the RS-EPI trajectory. In (A), an undistorted FSE image is shown for anatomic reference.

2.3.5 CONCLUSION

The susceptibility variations around the spine cause significant distortions in EPI images, making it difficult to obtain quantitative images of the spinal cord. Luckily, there is an arsenal of techniques that can be used to provide high-quality quantitative spine images. These techniques, some of which are described in this chapter, can be further improved with the advent of

advanced spine-array and head and neck coils that can achieve high acceleration factors. Combining postprocessing distortion correction techniques (such as RGPM correction) with acquisition-based methods (such as rFOV imaging, RS-EPI, and parallel imaging), one may be able to "come close" to providing distortion-free spinal cord EPI-based images that are robust to motion.

References

1. Schenck JF. The role of magnetic susceptibility in magnetic resonance imaging: MRI magnetic compatibility of the first and second kinds. *Med Phys*. 1996;23(6):815–850.
2. Bammer R, Fazekas F. Diffusion imaging of the human spinal cord and the vertebral column. *Top Magn Reson Imaging*. 2003;14(6):461–476.
3. Cooke FJ, et al. Quantitative proton magnetic resonance spectroscopy of the cervical spinal cord. *Magn Reson Med*. 2004;51(6):1122–1128.
4. Fischer H, Ladebec R. Echo-planar imaging image artifacts. In: Schmitt F, Stehling MK, Turner R, eds. *Echo-Planar Imaging: Theory, Technique and Application*. Berlin: Springer-Verlag; 1998:179–200.
5. Delfaut EM, et al. Fat suppression in MR imaging: techniques and pitfalls. *Radiographics*. 1999;19(2):373–382.
6. Bammer R, et al. Diffusion-weighted MR imaging of the spinal cord. *AJNR Am J Neuroradiol*. 2000;21(3):587–591.
7. Ries M, et al. Diffusion tensor MRI of the spinal cord. *Magn Reson Med*. 2000;44(6):884–892.
8. Bammer R, et al. Diffusion-weighted imaging of the spinal cord: interleaved echo-planar imaging is superior to fast spin-echo. *J Magn Reson Imaging*. 2002;15(4):364–373.
9. Wheeler-Kingshott CAM, et al. Investigating cervical spinal cord structure using axial diffusion tensor imaging. *NeuroImage*. 2002;16(1):93–102.
10. Wilm BJ, et al. Reduced field-of-view MRI using outer volume suppression for spinal cord diffusion imaging. *Magn Reson Med*. 2007;57(3):625–630.
11. Saritas EU, et al. DWI of the spinal cord with reduced FOV single-shot EPI. *Magn Reson Med*. 2008;60(2):468–473.
12. Dowell NG, et al. Contiguous-slice zonally oblique multislice (CO-ZOOM) diffusion tensor imaging: examples of in vivo spinal cord and optic nerve applications. *J Magn Reson Imaging*. 2009;29(2):454–460.
13. Tsuchiya K, et al. Diffusion-weighted MRI of the cervical spinal cord using a single-shot fast spin-echo technique: findings in normal subjects and in myelomalacia. *Neuroradiology*. 2003;45(2):90–94.
14. Tsuchiya K, Fujikawa A, Suzuki Y. Diffusion tractography of the cervical spinal cord by using parallel imaging. *AJNR Am J Neuroradiol*. 2005;26(2):398–400.
15. Cercignani M, et al. Sensitivity-encoded diffusion tensor MR imaging of the cervical cord. *AJNR Am J Neuroradiol*. 2003;24(6):1254–1256.
16. Zaharchuk G, et al. Reduced field-of-view diffusion jmaging of the human spinal cord: comparison with conventional single-shot echo-planar imaging. *AJNR Am J Neuroradiol*. 2011;32(5):813–820.
17. Jeong EK, et al. High-resolution DTI with 2D interleaved multislice reduced FOV single-shot diffusion-weighted EPI (2D ss-rFOV-DWEPI). *Magn Reson Med*. 2005;54(6):1575–1579.
18. Finsterbusch J. High-resolution diffusion tensor imaging with inner field-of-view EPI. *AJNR Am J Neuroradiol*. 2009;29(4):987–993.
19. Griswold MA, et al. Generalized autocalibrating partially parallel acquisitions (GRAPPA). *Magn Reson Med*. 2002;47(6):1202–1210.
20. Pruessmann KP, et al. SENSE: sensitivity encoding for fast MRI. *Magn Reson Med*. 1999;42(5):952–962.
21. Maieron M, et al. Functional responses in the human spinal cord during willed motor actions: evidence for side- and rate-dependent activity. *J Neurosci*. 2007;27(15):4182–4190.
22. Cohen-Adad J, et al. 32-Channel RF coil optimized for brain and cervical spinal cord at 3 T. *Magn Reson Med*. 2011;66(4):1198–1208.
23. Mckinnon GC. Ultrafast interleaved gradient-echo-planar imaging on a standard scanner. *Magn Reson Med*. 1993;30(5):609–616.
24. Thurnher MM, Bammer R. Diffusion-weighted MR imaging (DWI) in spinal cord ischemia. *Neuroradiology*. 2006;48(11):795–801.
25. Plank C, et al. Diffusion-weighted MR imaging (DWI) in the evaluation of epidural spinal lesions. *Neuroradiology*. 2007;49(12):977–985.
26. Demir A, et al. Diffusion-weighted MR imaging with apparent diffusion coefficient and apparent diffusion tensor maps in cervical spondylotic myelopathy. *Radiology*. 2003;229(1):37–43.
27. Summers P, et al. A preliminary study of the effects of trigger timing on diffusion tensor imaging of the human spinal cord. *AJNR Am J Neuroradiol*. 2006;27(9):1952–1961.
28. Holder CA, et al. Diffusion-weighted MR imaging of the normal human spinal cord in vivo. *AJNR Am J Neuroradiol*. 2000;21(10):1799–1806.
29. Feinberg DA, Oshio K. Phase errors in multishot echo-planar imaging. *Magn Reson Med*. 1994;32(4):535–539.
30. Decrespigny AJ, et al. Navigated diffusion imaging of normal and ischemic human brain. *Magn Reson Med*. 1995;33(5):720–728.
31. Butts K, et al. Diffusion-weighted interleaved echo-planar imaging with a pair of orthogonal navigator echoes. *Magn Reson Med*. 1996;35(5):763–770.
32. Porter DA, Heidemann RM. High resolution diffusion-weighted imaging using readout-segmented echo-planar imaging, parallel imaging and a two-dimensional navigator-based reacquisition. *Magn Reson Med*. 2009;62(2):468–475.
33. Holdsworth SJ, et al. Robust GRAPPA-accelerated diffusion-weighted readout-segmented (RS)-EPI. *Magn Reson Med*. 2009;62(6):1629–1640.
34. Gudbjartsson H, et al. Line scan diffusion imaging. *Magn Reson Med*. 1996;36(4):509–519.
35. Finsterbusch J, Frahm J. Diffusion-weighted single-shot line scan imaging of the human brain. *Magn Reson Med*. 1999;42(4):772–778.
36. Finsterbusch J, Frahm J. Diffusion tensor mapping of the human brain using single-shot line scan imaging. *J Magn Reson Imaging*. 2000;12(3):388–394.
37. Kubicki M, et al. Comparison of single-shot echo-planar and line scan protocols for diffusion tensor imaging. *Acad Radiol*. 2004;11(2):224–232.
38. Robertson RL, et al. MR line-scan diffusion imaging of the spinal cord in children. *AJNR Am J Neuroradiol*. 2000;21(7):1344–1348.
39. Maier SE. Examination of spinal cord tissue architecture with magnetic resonance diffusion tensor imaging. *Neurotherapeutics*. 2007;4(3):453–459.
40. Maier SE, Mamata H. Diffusion tensor imaging of the spinal cord. *Ann N Y Acad Sci*. 2005;1064:50–60.
41. Mamata H, et al. Collateral nerve fibers in human spinal cord: visualization with magnetic resonance diffusion tensor imaging. *NeuroImage*. 2006;31(1):24–30.
42. Bammer R, et al. Line scan diffusion imaging of the spine. *AJNR Am J Neuroradiol*. 2003;24(1):5–12.
43. Hennig J, Nauerth A, Friedburg H. RARE imaging: a fast imaging method for clinical MR. *Magn Reson Med*. 1986;3(6):823–833.
44. Xu D, et al. Single-shot fast spin-echo diffusion tensor imaging of the brain and spine with head and phased array coils at 1.5 T and 3.0 T. *Magn Reson Imaging*. 2004;22(6):751–759.

45. Sarlls JE, et al. Isotropic diffusion weighting in radial fast spin-echo magnetic resonance imaging. *Magn Reson Med*. 2005; 53(6):1347–1354.
46. Dietrich O, et al. Diffusion-weighted imaging of the spine using radial k-space trajectories. *Magma*. 2001;12(1):23–31.
47. Bernstein M, King K, Zhou X. Handbook of MRI Pulse Sequences. In: E.A. Press, ed. Elsevier Academic Press; 2004, 1040.
48. Pipe JG. Motion correction with PROPELLER MRI: application to head motion and free-breathing cardiac imaging. *Magn Reson Med*. 1999;42(5):963–969.
49. Pipe JG, Zwart N. Turboprop: improved PROPELLER imaging. *Magn Reson Med*. 2006;55(2):380–385.
50. Deng J, Omary RA, Larson AC. Multishot diffusion-weighted SPLICE PROPELLER MRI of the abdomen. *Magn Reson Med*. 2008;59(5):947–953.
51. Wang FN, et al. PROPELLER EPI: an MRI technique suitable for diffusion tensor imaging at high field strength with reduced geometric distortions. *Magn Reson Med*. 2005;54(5):1232–1240.
52. Sarlls J, Pierpaoli C. High-resolution diffusion tensor imaging at 3T with radial-FSE. *Proceedings of the 16th Annual Meeting of ISMRM*. Toronto, Canada; 2008.
53. Sarlls JE, Pierpaoli C. Diffusion-weighted radial fast spin-echo for high-resolution diffusion tensor imaging at 3T. *Magn Reson Med*. 2008;60(2):270–276.
54. Ellingson BM, Sulaiman O, Kurpad SN. High-resolution in vivo diffusion tensor imaging of the injured cat spinal cord using self-navigated, interleaved, variable-density spiral acquisition (SNAILS-DTI). *Magn Reson Imaging*. 2010;28(9):1353–1360.
55. Cohen-Adad J, et al. BOLD signal responses to controlled hypercapnia in human spinal cord. *NeuroImage*. 2010;50(3):1074–1084.
56. Eilenberg SS, Tartar VM, Mattrey RF. Reducing magnetic-susceptibility differences using liquid fluorocarbon pads (Sat Pad(Tm))—results with spectral presaturation of fat. *Artif Cells Blood Substitutes Immobilization Biotechnol*. 1994;22(4):1477–1483.
57. Rosen Y, et al. 3T MR of the prostate: reducing susceptibility gradients by inflating the endorectal coil with a barium sulfate suspension. *Magn Reson Med*. 2007;57(5):898–904.
58. Mitchell DG, et al. Comparison of Kaopectate with barium for negative and positive enteric contrast at MR imaging. *Radiology*. 1991;181(2):475–480.
59. Lee GC, et al. Pyrolytic graphite foam: a passive magnetic susceptibility matching material. *J Magn Reson Imaging*. 2010;32(3): 684–691.
60. Schneider E, Glover G. Rapid in vivo proton shimming. *Magn Reson Med*. 1991;18(2):335–347.
61. Robson MD, Gore JC, Constable RT. Measurement of the point spread function in MRI using constant time imaging. *Magn Reson Med*. 1997;38(5):733–740.
62. Jezzard P, Balaban RS. Correction for geometric distortion in echo-planar images from B-0 field variations. *Magn Reson Med*. 1995;34(1):65–73.
63. Cusack R, Brett M, Osswald K. An evaluation of the use of magnetic field maps to undistort echo-planar images. *NeuroImage*. 2003;18(1):127–142.
64. Reber PJ, et al. Correction of off resonance-related distortion in echo-planar imaging using EPI-based field maps. *Magn Reson Med*. 1998;39(2):328–330.
65. Chang H, Fitzpatrick JM. A technique for accurate magnetic-resonance-imaging in the presence of field inhomogeneities. *IEEE Trans Med Imaging*. 1992;11(3):319–329.
66. Andersson JLR, Skare S, Ashburner J. How to correct susceptibility distortions in spin-echo echo-planar images: application to diffusion tensor imaging. *NeuroImage*. 2003;20(2):870–888.
67. Skare S, Andersson JLR. Correction of MR image distortions induced by metallic objects using a 3D cubic B-spline basis set: application to stereotactic surgical planning. *Magn Reson Med*. 2005;54(1):169–181.
68. Kannengiesser SAR, Wang Y, Haacke EM. Geometric distortion correction in gradient-echo imaging by use of dynamic time warping. *Magn Reson Med*. 1999;42(3):585–590.
69. Bowtell RMD, Commandre MJ, Glover PM. Correction of geometric distortions in echo planar images. *Proceedings of the 2nd Annual Meeting of ISMRM*. San Francisco, CA; 1994.
70. Ardekani S, Sinha U. Geometric distortion correction of high-resolution 3 T diffusion tensor brain images. *Magn Reson Med*. 2005;54(5):1163–1171.
71. Villain N, et al. A simple way to improve anatomical mapping of functional brain imaging. *J Neuroimaging*. 2010;20(4):324–333.
72. Cohen-Adad J, Lundell H, Rossignol S. Distortion correction in spinal cord DTI: what's the best approach? *Proceedings of the 17th Scientific Meeting of ISMRM*. Honolulu, HI, USA; 2009:3178.
73. Jenkinson M. Fast, automated, N-dimensional phase-unwrapping algorithm. *Magn Reson Med*. 2003;49(1):193–197.
74. Lundell H, et al. Fast diffusion tensor imaging and tractography of the whole cervical spinal cord using point spread function corrected echo planar imaging. *Magn Reson Med*. 2013;69(1): 144–149.
75. Andersson JSS, Skare ST. Image distortion and its correction in diffusion MRI. In: J DK, ed. *Diffusion MRI: Theory, Methods, and Applications*. Oxford University Press; 2010:285–302.